A&A, 692, A152 (2024)
https://doi.org/10.1051/0004-6361/202452148

Astronomy & Astrophysics

H_2–H_2O demixing in Uranus and Neptune: Adiabatic structure models

M. Cano Amoros[1,⋆], N. Nettelmann[2], N. Tosi[1], P. Baumeister[3], and H. Rauer[1]

[1] Institute of Planetary Research, German Aerospace Center (DLR), Rutherfordstr. 2, Berlin 12489, Germany
[2] Department of Astronomy and Astrophysics, University of California UCSC), High St 1156, Santa Cruz, CA 95064, USA
[3] Department of Earth Sciences, Freie Universität Berlin (FU), Malteserstr. 74-100, Berlin 12249, Germany

Received 6 September 2024 / Accepted 25 October 2024

ABSTRACT

Context. Demixing properties of major planetary constituents influence the interior structure and evolution of planets. Comparing experimental and computational data on the miscibility of hydrogen and water to adiabatic profiles suggests that phase separation between these two components occurs in the ice giants Uranus and Neptune.
Aims. We aim to predict the atmospheric water abundance and transition pressure between the water-poor outer envelope and the water-rich deep interior in Uranus and Neptune.
Methods. We constructed seven H_2–H_2O phase diagrams from the available experimental and computational data. We computed interior adiabatic structure models and compared these to the phase diagrams to infer whether demixing occurred.
Results. We obtain a strong water depletion in the top layer due to the rain-out of water and find upper limits on the atmospheric water-mass fraction $Z_{\rm atm}$ of 0.21 for Uranus and 0.16 for Neptune. The transition from the water-poor to the water-rich layer is sharp and occurs at pressures P_Z between 4 and 11 GPa. Using these constraints on $Z_{\rm atm}$ and P_Z, we find that the observed gravitational harmonics J_2 and J_4 can be reproduced if $P_Z \gtrsim 10$ GPa in Uranus and $\gtrsim$5 GPa in Neptune, and if the deep interior has a high primordial water-mass fraction of 0.8, unless rocks are also present. The agreement with J_4 is improved if rocks are confined deeper than P_Z, for instance, below a rock cloud level at 2000 K (20–30 GPa).
Conclusions. These findings confirm classical few-layer models and suggest that a layered structure may result from a combination of primordial mass accretion and subsequent phase separation. Reduced observational uncertainty in J_4 and its dynamic contribution, atmospheric water abundance measurements from the Uranus Orbiter and Probe (UOP) or a Neptune mission, and better understanding of the mixing behaviour of constituents are needed to constrain the interiors of ice giants.

Key words. planets and satellites: composition – planets and satellites: formation – planets and satellites: interiors

1. Introduction

To understand the origin of the Solar System and how planets form, it is important to unveil the mysteries surrounding the interiors of the outer planets Uranus and Neptune, as they are giant reservoirs of the planet building blocks in the early outer Solar System. Modelling their interior structure is one step in that direction. Uranus and Neptune are termed ice giants because their deep interior densities are consistent with that of a compressed mix of the ice-forming volatiles water, methane, and ammonia, or even 'water only' if hydrogen-rich gas is assumed to be present in their deep interiors as well. Oxygen (O) and carbon (C) are the next most abundant elements after hydrogen (H) and helium (He) in the protosolar disc gas. They condense to water or CO ice in the outer regions of protosolar discs (Mousis et al. 2024). If exposed to accreted H-rich gas, C and O react to form the 'ices' water and methane. Therefore, the chemistry and phase diagrams of H, O, and C-mixtures are expected to be important for understanding ice giant interiors.

Interior structure models are constrained by observations, mainly by planetary mass, radius, atmospheric temperature, gravitational harmonics, and rotation rate. For the ice giants, the accuracy of these quantities is still limited compared to the gas giants Jupiter and Saturn. With Juno and the Cassini Grand Finale Tour, the gas giants each had their dedicated orbiter missions to measure the gravity field (Bolton et al. 2017; Iess et al. 2019). On Jupiter, the Galileo entry probe measured atmospheric composition. In contrast, the ice giants have only been visited by a single Voyager 2 flyby each.

Currently, Uranus and Neptune models point towards an H/He-rich atmosphere and a deeper interior enriched in heavy elements (Helled et al. 2020). This outcome of interior models is robust and independent of the approach used to infer the interior mass distribution. Two main approaches can be defined. One approach assumes an adiabatic interior, consisting of distinct layers, usually a core composed of rocks, an ice-rich layer surrounding the core that primarily consists of O and H, and a top layer composed primarily of H and He (Hubbard & MacFarlane 1980; Nettelmann et al. 2013). The ice-rich layer may also contain the rock-forming elements Si, Mg, and Fe, or other volatiles such as C, N, and S if they are miscible (Vazan et al. 2022). Physical equations of state (EoS) are used to describe the behaviour of these elements or their compounds at relevant pressure and temperature conditions. Another approach is to adopt empirical structure models without making a priori assumptions on the composition, using density profiles described by high-order polynomials (Helled et al. 2010a; Movshovitz et al. 2020), polytropes (Neuenschwander & Helled 2022; Neuenschwander et al. 2024), or random monotonic functions (Podolak et al. 2022).

⋆ Corresponding author; marina.canoamoros@dlr.de

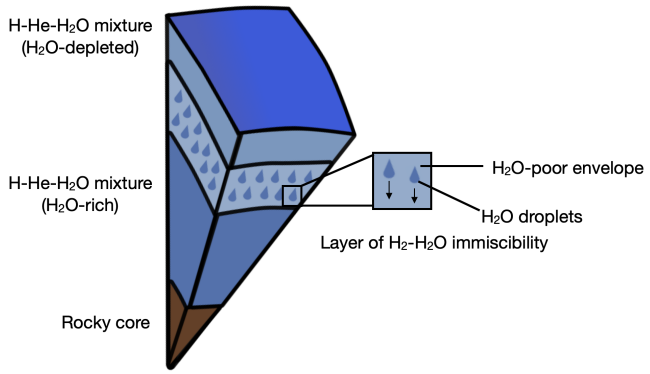

Fig. 1. Illustration of interior of an ice-giant-like planet with a H_2–H_2O immiscibility layer and water-rich droplets sinking and enriching the deeper envelope while leaving behind a water-depleted, hydrogen-rich top layer. This illustration also applies to He rain in a gas-giant planet, as shown in Militzer et al. (2016).

The latter method facilitates the possibility of considering more complex structures, including compositional gradients and non-adiabatic interiors (Neuenschwander et al. 2024; Malamud et al. 2024). However, even if the profiles match observations, relating these profiles to physical EoSs remains challenging.

Regardless of the method used, several open questions remain that require physical principles to confirm, exclude, and justify possible density profiles such as whether layers undergo gradual transitions, whether the P–T profiles are adiabatic implying convection, or even whether the ice giants are water-rich at all or perhaps rock-dominated with H-gas to reduce the density where needed instead (Helled & Fortney 2020). At any rate, all approaches consistently predict the outer parts of the two ice giants to have a lower metallicity (Z) than the deeper interior, which is rich in heavy elements. Explaining such a structure by physical principles is important for understanding the formation and evolution of the planets.

Bailey & Stevenson (2021) provide a physical explanation for the traditional three-layer structure. They suggest that immiscibility (or demixing) between molecular hydrogen and water leads to a sharp compositional transition (Fig. 1). To fit the gravitational harmonics, they find that Neptune requires a water abundance at least an order of magnitude higher in the top H-dominated envelope compared to Uranus. The authors explain this discrepancy by hypothesising that Neptune may be in an earlier phase of H_2–H_2O demixing, while Uranus would already be fully differentiated. Consequently, Neptune could be experiencing gravitational energy release of sufficient magnitude to account for its high heat flow today, thereby offering a plausible explanation for the observed dichotomy in the luminosities between the ice giants (Pearl et al. 1990; Pearl & Conrath 1991).

Demixing is an important process on other planets, on Jupiter for instance, where the separation of helium from metallic hydrogen at megabar pressures and subsequent He rain under the influence of gravity can explain the observed atmospheric helium and neon depletion (von Zahn et al. 1998; Wilson & Militzer 2010). However, experimental data on H–He demixing at megabar pressures are sparse, and gas giant models rely on theoretical H-He phase diagrams with large uncertainties in the demixing temperature ($T_{\rm dmx}$) of the order of 1000 K.

The mechanism proposed by Bailey & Stevenson (2021) for H_2–H_2O demixing in the ice giants is based on experimental data of the immiscibility of H_2–H_2O mixtures up to 3 GPa (Seward & Franck 1981; Bali et al. 2013). Based on these data, Bailey & Stevenson (2021) constructed a H_2–H_2O phase diagram and found that their ice giants' adiabats were warmer than the phase boundary from the experimental data. Only upon linear extrapolation of this phase boundary beyond 3 GPa were Bailey & Stevenson (2021) able to find an intersection between the adiabats and the demixing curve, with consequent demixing in the interiors of Uranus and Neptune.

Subsequent to Bali et al. (2013), Vlasov et al. (2023) conducted experiments on H_2–H_2O miscibility up to 4.5 GPa, and Bergermann et al. (2024) used DFT-MD simulations to obtain the H_2–H_2O phase diagram. Here, we used these new results as input to follow up on the proposal by Bailey & Stevenson (2021) that H_2–H_2O demixing may shape the structure of the ice giants that is suggested by the gravity data.

We constructed phase diagrams constrained by the new data and various extrapolations thereof. By computing the equilibrium water abundance on the phase boundary, we predicted the atmospheric water abundance $Z_{\rm atm}$ at the bottom of the water cloud deck. We determined the water-poor-water-rich transition pressure (P_Z) in the planet and constructed interior structure models for Uranus and Neptune constrained by $Z_{\rm atm}$ and P_Z to compare with the observed gravity data. We find that rain-out can happen in the interiors of Uranus and Neptune, and our inferred outer-envelope water abundance and transition pressure leads to interior structures that can match the gravity harmonics.

The remainder of the paper is organised as follows. Section 2 describes our construction of H_2–H_2O phase diagrams from the experimental and theoretical data. In Sect. 3, we apply these diagrams to predict $Z_{\rm atm}$ and P_Z. Section 4 presents Uranus and Neptune structure models constrained by $Z_{\rm atm}$ and P_Z for comparison to their observed gravity field. In Sect. 5, we discuss our results, and we finish with a summary of the conclusions in Sect. 6. In the appendix, we present the systematic behaviour of the model gravitational harmonics upon variation of free parameters.

2. H_2–H_2O phase separation under ice giant P–T conditions

2.1. Ice-giant adiabats

We assumed adiabatic P–T profiles for an envelope composed of hydrogen, helium, and water, which became divided into an inner and an outer part due to H_2–H_2O demixing. These profiles were obtained starting at a pressure level of 1 bar and a corresponding surface temperature of $T_{1\,\rm bar} = T(P = 1\ \rm bar)$. For hydrogen, we used the effective H EoS, and for helium we used the pure He EoS by Chabrier & Debras (2021), which combines semi-analytical EoS models with ab initio molecular dynamics. In comparison to Chabrier et al. (2019), these updated EoSs account for interactions between H and He. We added H_2O to the mixture using the AQUA EoS from Haldemann et al. (2020), which is a combination of various EoSs and covers a wide pressure and temperature range (0.1 Pa to 400 TPa and 100 to 10^5 K).

The three tabulated EoSs were mixed using the additive volume rule. Following Eqs. (9)–(11) from Chabrier et al. (2019), for mass abundances X, Y, and Z of H, He, and H_2O, respectively, we calculated the ideal mixing entropy to obtain the specific entropy of the mixture. Based on the computed mixture, we calculated the adiabat by interpolating the entropy $S(T, P, X_i)$ for a mixture X_i starting at a given value of $T_{1\,\rm bar}$. As the tables do not cover temperatures lower than 100 K, we employed ideal gas EoSs for H, He, and H_2O for $T_{1\,\rm bar} < 100$ K as done by Scheibe et al. (2019). Compared to the physical EoSs of

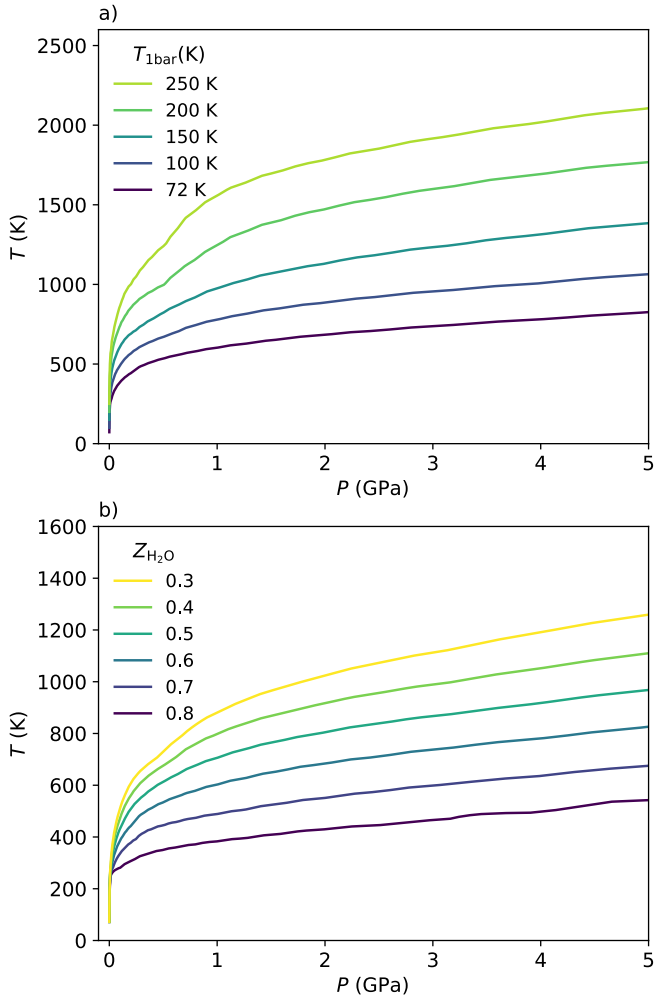

Fig. 2. Adiabatic temperature profiles for (a) different surface temperatures $T_{1\,bar}$ and fixed Z_{H_2O} = 0.6 and (b) different Z_{H_2O}, with $T_{1\,bar}$ fixed at Neptune's value of 72 K. For each case, the He/H ratio was kept protosolar.

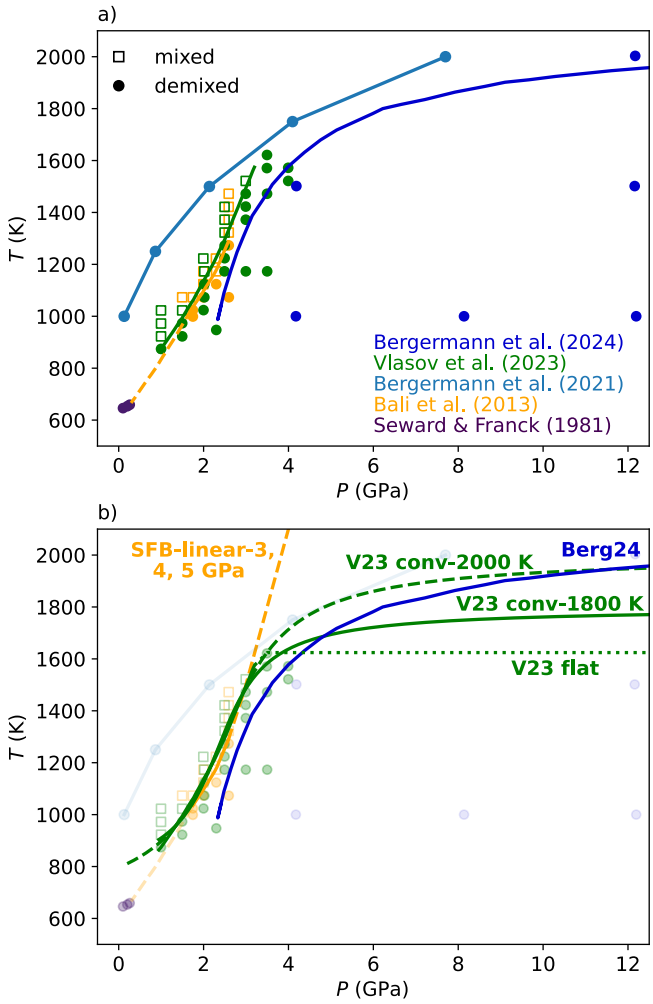

Fig. 3. Experimental data and theoretical predictions on H_2–H_2O miscibility. (a) Experimental data for 1:1 H_2–H_2O miscibility from Seward & Franck (1981) (purple), Bali et al. (2013) (yellow), and Vlasov et al. (2023) (green); and the computational predictions of Bergermann et al. (2021) (light blue curve) and Bergermann et al. (2024) (blue curve). Filled symbols correspond to the coexistence of two phases, while empty squares refer to complete mixing of H_2 and H_2O. The solid lines indicate the fit of the corresponding data points. (b) Extrapolated critical curves based on the data shown in panel a) and used to construct the phase diagrams (see text for details). The linear extrapolations of the data by Bali et al. (2013) beyond 3 GPa and up to 4 and 5 GPa are shown by the dashed yellow line. The three different extensions beyond 3.5 GPa for the Vlasov et al. (2023) data (flat, V23 conv-1800 K, and V23 conv-2000 K) are shown by green dotted, solid, and dashed lines, respectively. Finally, the blue curve is from Bergermann et al. (2024).

Chabrier & Debras (2021), the ideal gas approximation is appropriate at pressures of ∼1–100 bar. We set the switch to non-ideal EoSs at 10 bar since this pressure level was found to produce smooth P–T profiles and the temperatures along the adiabats have passed the 100 K threshold. For the iron-rock core, we used the pressure-density relation of Hubbard & Marley (1989) for an Earth-like bulk abundance of 38% SiO_2, 25% MgO, 25% FeS, and 12% FeO by mass.

Figure 2 shows examples of adiabatic profiles for different values of $T_{1\,bar}$ between 72 K and 250 K and a fixed water mass fraction Z_{H_2O} = 0.6 (Fig. 2a), or for Neptune's surface temperature of $T_{1\,bar}$ = 72 K, but varying the water-mass fraction between 0.3 and 0.8 (Fig. 2b). Figure 2 shows that higher water abundances lead to colder adiabats and that the change in the gradient is strongest at pressures below ∼1 GPa. The behaviour of the adiabats with increasing water abundance can be explained by the inverse relation between the adiabatic gradient and the specific heat capacity, which is larger for molecules with higher degrees of freedom.

2.2. Construction of H_2–H_2O phase diagrams

To construct an H_2–H_2O phase diagram, we relied on experimental immiscibility data from Seward & Franck (1981), Bali et al. (2013), and Vlasov et al. (2023), as well as on theoretical predictions by Bergermann et al. (2021) and Bergermann et al. (2024). This collection of data is shown in Fig. 3a.

Seward & Franck (1981) (hereafter SF81) studied the immiscibility of H_2–H_2O up to 2500 bar (0.25 GPa) and 440 °C. They conducted isochoric experiments for H_2–H_2O mixtures ranging from hydrogen-poor (0.5 mol%) to hydrogen-rich (90 mol%) using a pressure vessel. The critical, or demixing, temperature (T_{dmx}) is the maximum temperature at which a mixture can coexist as two distinct phases, with higher temperatures leading to complete mixing. Figure 3a shows the critical T_{dmx} points of Seward & Franck (1981) at 0.1, 0.2, and 0.25 GPa for a 1:1 H_2–H_2O bulk mixture in purple.

Bali et al. (2013) (hereafter B13) conducted experiments at higher pressures than SF81 using the synthetic fluid inclusion method. By trapping fluids in silicate minerals, they study the immiscibility of a 1:1 H_2–H_2O mixture up to 3 GPa. They inferred the location of the critical curve for the mixture by visually inspecting the inclusion type and confirming its composition with Raman spectroscopy. Inclusions containing both an H_2- and an H_2O-rich phase were interpreted as cases of full miscibility, while compositionally different inclusions were interpreted as cases of immiscibility. Their experimental data are shown in Fig. 3a as yellow dots, and their fit is represented by the solid yellow line.

We used the above-mentioned experimental data to construct the first three of our demixing curves $T_{\rm dmx}(P)$ for a 1:1 mixture. Figure 3a shows that the critical temperatures of SF81 connect well to the data of B13 with a dashed yellow line, as also shown by Bailey & Stevenson (2021). The curve is nearly linear, with a slight change in slope between 2.5 and 3 GPa. As in Bailey & Stevenson (2021), to reach conditions at higher pressures relevant to the ice giants' interiors, we linearly extrapolated this 1:1 critical curve towards higher pressures beyond 3 GPa. We cut off the critical curves at 3 GPa (no extrapolation), 4 GPa, and 5 GPa, and we label the three corresponding phase boundaries and subsequent phase diagrams as 'SFB-linear-3 GPa', and so on. The cut-off implies that we assume miscibility at higher pressures beyond the respective cut-off pressure. These extrapolated critical curves are shown in Fig. 3b. They serve to compare our results with those of Bailey & Stevenson (2021) and to explore the response of the models in the absence of experimental data beyond 3 GPa, that is prior to the arrival of the Vlasov data.

More recently, Vlasov et al. (2023) (hereafter V23) obtained new experimental data for the critical curve of the H_2–H_2O system up to 3.5 GPa and 1400 °C following the same method as Bali et al. (2013). For 4 GPa, they only provide a lower limit to the critical temperature. At ∼3.5 GPa, their data indicate a flattening of the critical curve. We used this additional information to construct three more improved critical curves $T_{\rm dmx}(P)$ beyond 4 GPa. First, we took a 'flat' case, for which we extended the curve horizontally from the last critical temperature measurement at ∼3.5 GPa towards higher pressure levels. This yields the lowest possible $T_{\rm dmx}(P)$ 1:1 curve. Additionally, we aim to approximate the change of slope indicated by the V23 data and the theoretical prediction of Bergermann et al. (2021) (see next paragraph). To do so, we fit the experimental data of B13 and V23 by an arctan function that approaches either 1800 K at high pressures (case 'V23 conv-1800 K') or 2000 K (case 'V23 conv-2000 K'). In contrast to the linear extrapolations, these three critical curves are consistent with the theoretical predictions by Bergermann et al. (2021).

Bergermann et al. (2021) performed Gibbs ensemble Monte Carlo simulations up to 8 GPa and 2000 K with analytical pair-potentials for the interaction between the molecular species. This approach neglects the variable electronic structure of the molecules, which they suggest is what leads to the difference with the data of Bali et al. (2013). In contrast, in Bergermann et al. (2024) (hereafter Berg24), DFT-MD simulations were employed that do include the electronic structure within the density-functional theory for the electronic subsystem. This apparently leads to a downward shift in $T_{\rm dmx}$ and a good agreement with the experimental data at a few GPa. In both theoretical cases, the critical curves bend toward higher pressures and do not exceed 2000 K. Our V23 conv-1800 K and V23 conv-2000 K cases precede the Berg24 results and, as Fig. 3b shows, bracket the Berg24 curve at $P > 5$ GPa; they follow the experimental points between 2 and 3.5 GPa. Finally, we adopted the critical curve of Berg24. This critical curve is slightly off compared to the experimental data up to 3 GPa. However, as we show later, this low-pressure region does not influence our phase-separation results.

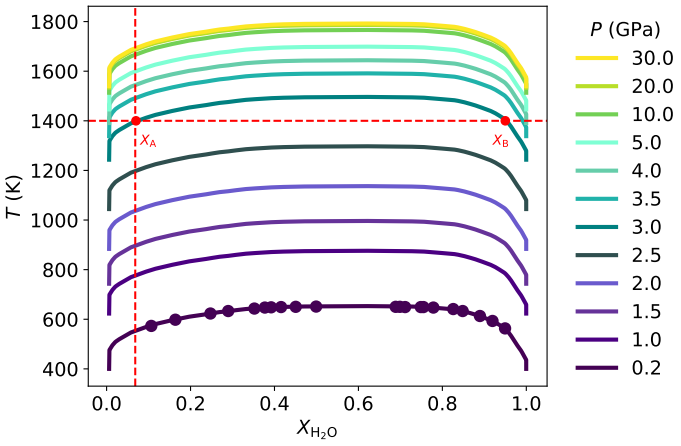

Fig. 4. Example of a phase diagram $T_{\rm dmx}(P, x_{\rm H_2O})$ based on the shape of the 0.2 GPa isobar according to the experimental data (purple points) of Seward & Franck (1981). Higher isobars are obtained by shifting the 0.2 GPa curve vertically according to the given critical curve $T_{\rm dmx}(P, 0.5)$. Here, the V23 conv-1800 K case is shown. x_A and x_B show the coexisting particle fractions at 3 GPa and 1400 K. The water-poor equilibrium abundance x_A is used to compute the atmospheric abundance.

In summary, we have seven critical curves at our disposal: SFB-linear-3, -4, -5 GPa, V23 flat, V23 conv-1800 K, V23 conv-2000 K, and Berg24. From these curves, we constructed seven H_2–H_2O phase diagrams. The shape of the phase diagram is based on results from Seward & Franck (1981). They found that the isobaric curve at 0.2 and 0.25 GPa becomes nearly symmetric around the 1:1 H_2–H_2O concentration, where $T_{\rm dmx}$ attains a maximum. This symmetric behaviour is observed at 0.2 and 0.25 GPa. The experimental data for the 0.2 GPa isobar is shown in purple dots in Fig. 4. The way we constructed phase diagrams from the sparse experimental or theoretical data described above was by assuming that the shape of the isobaric demixing curve observed at 0.2 GPa holds for all higher pressures considered. Therefore, given a point $T_{\rm dmx}(P, x_{\rm H_2O})$, for any higher pressure P and any water concentration $x_{\rm H_2O}$, we can readily draw the respective isobaric demixing curve $T_{\rm dmx}(P, x_{\rm H_2O})$ by shifting the baseline curve for 0.2 GPa upwards with temperature. An example of a resulting phase diagram is illustrated in Fig. 4 for the critical curve V23 conv-1800 K. In the same manner, we constructed phase diagrams for the rest of the critical curves. In the Berg24 case, a phase diagram consistent with the experimental data up to 3 GPa and the Berg24 curve beyond 4 GPa could also have been easily constructed via interpolation. However, we did not do this since this lower pressure region is above the region where phase separation occurs, as shown in Sect. 3.2.2.

2.3. Equilibrium water abundance

For a given adiabat $T_{\rm ad}(P, Z)$ of composition Z and protosolar ratio X/Y, constrained by $T_{1\,\rm bar}$, and a phase diagram $T_{\rm dmx}(P, Z)$, phase separation occurs when $T_{\rm ad}(P, Z) < T_{\rm dmx}(P, Z)$. Water-rich droplets rain out, and Z decreases until $T_{\rm ad}(P, Z_A) \geq T_{\rm dmx}(P, Z_A)$

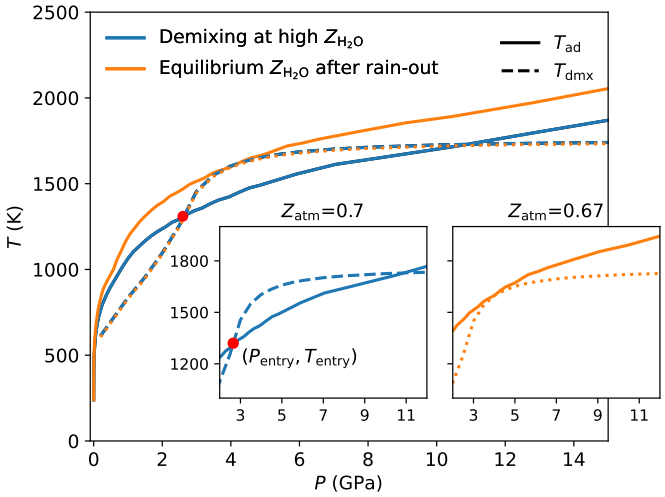

Fig. 5. Determination of water equilibrium abundance. Solid lines and dashed lines denote adiabats and demixing curves, respectively, the latter being obtained from the V23 conv-1800 K phase diagram shown in Fig. 4. We start with an overlap region where $T_{ad} < T_{dmx}$ and an initial water abundance of $Z = 0.7$ throughout the entire planet. Then, Z is decreased until the overlap region disappears and $T_{ad} \geq T_{dmx}$ at all pressures. Here, the equilibrium abundance found is 0.67. The orange adiabat is the profile with a 0.67 outer-envelope abundance. The obtained abundance is high in this example because $T_{1\,bar} = 240$ K, implying a rather warm adiabat in a young planet. The demixing region for the case with $Z_{atm} = 0.7$ is much larger compared to that typically encountered in our simulations. This choice was made for visual clarity (see text for more details).

at all pressures, where Z_A is the equilibrium mass fraction on the water-poor side of the phase diagram (see Fig. 4). Equality holds where the adiabat is tangential to the demixing curve, which typically occurs at a single pressure point but can also occur over an extended pressure region. We note that we use the 'Z' symbol for the mass fraction and 'x' for the particle fraction. Since in this work we only used water for the heavy elements, $Z = Z_{H_2O}$ and $x = x_{H_2O}$. The conversion between Z_{H_2O} and x_{H_2O} was done using Eq. (1). $T_{dmx}(P, x_{H_2O})$ is what is read from the phase diagram (Fig. 4) and converted into $T_{dmx}(P, Z_{H_2O})$. We then compared the adiabatic profile $T_{ad}(P, Y, Z)$ and the demixing curve $T_{dmx}(P, Z)$ to check whether demixing occurs and what the resulting equilibrium water abundance due to rain-out is. In Fig. 4, the equilibrium composition x_A on the water-poor side of the phase boundary is shown for an example pressure of 3 GPa and temperature of 1400 K. To determine x_A (or Z_A), we implemented a new procedure in our interior structure code TATOOINE (see Sect. 3.1), which is similar to the procedure adopted by Nettelmann et al. (2015) and Nettelmann et al. (2024) to treat H–He demixing.

In the case of H-He phase separation, both the adiabat and the demixing curve become colder with decreasing He-abundance but at a different rate, which is how, in that case, an equilibrium He-abundance can be found. Here, upon water rain-out, the adiabat becomes warmer, while the demixing curve changes little. This behaviour is illustrated in Fig. 5. For a high water abundance $Z = 0.7$ (blue curves), a wide overlap region exists where $T_{ad} < T_{dmx}$. From the pressure at the entry of the overlap region (P_{entry}), we obtained a new isobar of our phase diagram by interpolation. From the corresponding temperature (T_{entry}), we obtained the two co-existing abundances, x_A and x_B in particle fraction (as shown in Fig. 4), or Z_A and Z_B in mass fraction as follows:

$$Z_{H_2O} = \frac{9\, x_{H_2O}}{1 + 8\, x_{H_2O}}, \tag{1}$$

which is valid only in the absence of He. In the presence of He with a protosolar mass fraction Y, we have

$$Z_{H_2O} = \frac{m_{H_2O}\, O/H}{m_{H_2O}\, O/H + m_{He}\, He/H + m_H\, (1 - 2O/H)}, \tag{2}$$

with

$$He/H = \frac{He/H_{free}}{1 + 2O/H_{free}}, \tag{3}$$

$$He/H_{free} = \frac{Y}{1 - Y}\,\frac{m_H}{m_{He}}, \tag{4}$$

$$O/H_{free} = \frac{O/H}{1 - 2O/H}, \tag{5}$$

where H_{free} refers to H atoms that are free or bound in H_2, while H in X/H refers to all H atoms. We took Z_A as the new water abundance of the adiabat.

With a lower Z in the outer envelope, the new adiabat is slightly warmer. We repeated the whole procedure iteratively until T_{ad} and T_{dmx} intersect only once, as shown in Fig. 5 by the orange curves. We went from having an overlap region between T_{ad} and T_{dmx} with $Z = 0.7$ to the point where $T_{ad} \approx T_{dmx}$ when water has rained out and the water abundance has decreased to the equilibrium value $Z = 0.67$. We point out that the adiabats in Fig. 5 do not show two consecutive steps in our procedure. Since we start our procedure at the first instance in temperature where demixing can occur, we never have such a large demixing region as that shown in the 0.7 case, because we are always close to equilibrium. Therefore, the exaggerated temperature increase that can be seen here does not actually occur.

Furthermore, one can see from the dashed lines in Fig. 5 that the change in the demixing curve with Z is tiny. This can be explained by the rather flat behaviour of the isobars in the phase diagram throughout most of the compositional range (see Fig. 4). We took this equilibrium abundance as the atmospheric water abundance (Z_{atm}). In this way, we assumed that convection will cause mixing of all material above the rain-region; thus, the top envelope will adopt this abundance because the convective overturn happens faster than the rain-out in this region.

3. Models based on H_2–H_2O phase diagrams

We computed four kinds of structure models: (i) models where the atmospheric water abundance Z_{atm} and the transition pressure P_Z are constrained by the H_2–H_2O phase diagrams; (ii) models where, in addition, the deep interior water abundance is constrained by the gravitational harmonic J_2; (iii) models also constrained by J_2, but with water and rocks in the deep interior above the core; and (iv) models that are constrained by J_2 only. In Sect. 3.1, we describe case (i) models; their results are given in Sect. 3.2. Models of cases (ii-iv) are described in Sect. 4.1.

3.1. Structure models constrained by water rain-out

We followed the traditional approach of modelling the planet's interior assuming a layered structure (e.g. Nettelmann et al. 2013). We used the 1D interior structure code TATOOINE (Baumeister et al. 2020; MacKenzie, Jasmine et al. 2023;

Baumeister & Tosi 2023) to construct a planet consisting of an isothermal core and two adiabatic envelopes on top. The envelopes are composed of H and He in a protosolar ratio and H_2O. The model inputs are the planet mass, the mass fractions for each layer, and the equations of state (mentioned in Sect. 2.1) describing the properties of the relevant elements at high pressure and temperature conditions. TATOOINE numerically integrates the equations of mass continuity, Eq. (6), and hydrostatic equilibrium, Eq. (7), coupled with the equation of state, Eq. (8):

$$\frac{\mathrm{d}m(r)}{\mathrm{d}r} = 4\pi r^2 \rho(r) \,, \tag{6}$$

$$\frac{\mathrm{d}P(r)}{\mathrm{d}r} = -\frac{Gm(r)\rho(r)}{r^2} \,, \tag{7}$$

$$P(r) = f(\rho(r), T(r), c(r)) \,, \tag{8}$$

where r is the radius, m is the mass, ρ is the density, P is the pressure, T is the temperature, and c is the composition. The above equations are integrated iteratively from the top downwards until the final solution is obtained when the mass at the planet's centre reaches approximately zero. In these models, we fix the rock core mass at $2M_E$.

For any temperature at the top of the atmosphere (1 bar pressure level here) $T_{1\,\mathrm{bar}}$, we found the transition pressure, P_Z, between the water-poor and water-rich envelope. Given P_Z, for each $T_{1\,\mathrm{bar}}$ we determined Z_{atm} and the mass from the centre of the planet up to P_Z, $m_Z := m(P_Z)$ from the planet structure model. Envelope 1 extends between M_p and $m(P_Z)$, and envelope 2 begins at $m(P_Z)$. The first structure model is homogeneous; that is, $Z = Z_1 = Z_2$, where Z_1 and Z_2 denote the water abundances of envelopes 1 and 2, respectively. Once we found at what surface temperature demixing can start, all parameters were known and the model where phase separation starts could be computed. For a colder adiabat (i.e. a lower $T_{1\,\mathrm{bar}}$), $Z_1 < Z_2$ due to rain-out. The new Z_1 was determined from the phase diagram as described in Sect. 2.3. We computed the mass of water Δm_{H_2O} that had rained out from envelope 1 to envelope 2. Given the previous amounts of water in the two envelopes and the change Δm_{H_2O}, we computed the new value Z_2 according to bulk water-mass conservation. With these new abundances for the envelopes and P_Z, a new structure model was computed that yielded the new m_Z. This was done repeatedly for various $T_{1\,\mathrm{bar}}$ values. Two opposing effects affect m_Z: envelope 1 becomes less dense and warmer as it loses water. This tends to decrease m_Z. Second, m_Z would increase as the planet becomes more compact upon cooling (Nettelmann et al. 2013).

By repeating this procedure until the present-day $T_{1\,\mathrm{bar}}$ value is reached, these models provided the atmospheric water abundance and transition pressure for present Uranus and Neptune for the seven different H_2–H_2O phase diagrams. However, the deep interior Z is not directly constrained by the H_2–H_2O phase diagram, only its change according to mass conservation for an assumed initial homogeneous-Z was determined.

3.2. Results

3.2.1. Atmospheric water abundance

We estimated the atmospheric water abundance Z_{atm} for a range of 1 bar temperatures from the start of the demixing to the present-day temperatures, $T_{1\,\mathrm{bar}}$, of Uranus and Neptune, which is the only parameter by which Uranus and Neptune are distinguished here. Figure 6 shows Z_{atm} as a function of $T_{1\,\mathrm{bar}}$. There

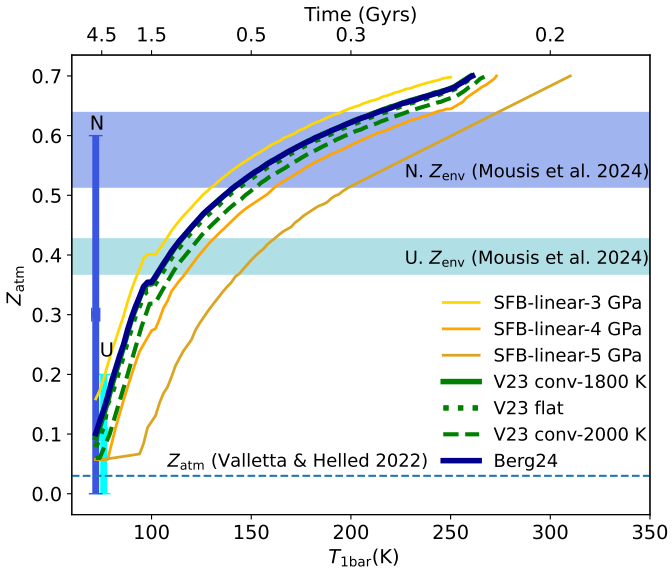

Fig. 6. Atmospheric water abundance as a function of $T_{1\,\mathrm{bar}}$ for each of the seven phase diagrams. The V23 conv-1800 K curve is hidden by the Berg24 curve. The change of slope near 100 K is due to the switch to the ideal-gas EoS for $T < 100$ K (see Sect. 2.1). Vertical uncertainty ranges on the left show the outer envelope water abundance from the structure models of Nettelmann et al. (2013). The top horizontal axis shows times corresponding to a model of Neptune's thermal evolution from Nettelmann et al. (2013). The dashed horizontal line shows the metallicity of the outer envelope found by Valletta & Helled (2022) using planet formation models. The horizontal shaded areas show the bulk oxygen enrichment predicted by Mousis et al. (2024) for the envelopes of Uranus and Neptune (Z_{env}), which we converted to mass fractions.

are seven curves, one for each of the seven constructed phase diagrams. The vertical error bars show the range of water abundance in the outer envelope of Uranus and Neptune obtained from three-layer structure models of Nettelmann et al. (2013).

We started with a warm planet with a mixed interior of an arbitrary initial water abundance $Z = 0.7$. As the planet cools, the atmospheric water abundance decreases due to the rain-out of water. The colder the adiabat, the more water rains out. The demixing process depletes the outer envelope of water whilst enriching the deeper interior. For Uranus ($T_{1\,\mathrm{bar}} = 76$ K), we find a range for the atmospheric water abundance Z_{atm} between 0.057 and 0.21. For Neptune ($T_{1\,\mathrm{bar}} = 72$ K), we obtain a range of Z_{atm} between 0.057 and 0.16. For comparison, in Fig. 6 we show the outer envelope heavy element metallicity from the formation models of Valletta & Helled (2022), which also only consider water. We also provide estimates of the bulk envelope oxygen enrichment from Mousis et al. (2024) converted into mass fractions using Eqs. (2)–(5). These estimates put our arbitrary initial water abundance into context with regards to formation models.

The timescale shown on the upper axis of Fig. 6 is based on the evolution models of Nettelmann et al. (2013) and suggests that phase separation may have started early in the evolution of these planets when $T_{1\,\mathrm{bar}}$ temperatures were around 300 K. Figure 6 shows the depletion of atmospheric water from the arbitrarily chosen starting abundance of 0.7. However, if the starting abundance were lower, as suggested by Mousis et al. (2024), demixing would start later on in the evolution of the planet, or earlier if the initial abundance were higher. This is due to the behaviour of the adiabat with water abundance, as shown in Fig. 2b. A higher initial water abundance will require a higher $T_{1\,\mathrm{bar}}$ for demixing to start. In any case, the final atmospheric water

abundance is independent of the starting initial abundance, Z. This is because the outer envelope abundance required for the adiabat and demixing curve to intersect only once is always the same for each $T_{1\,\mathrm{bar}}$. Therefore, to set a constraint on the deep interior water abundance based on our Z_{atm} predictions, interior structure models that are constrained by the observed gravitational harmonics are required.

3.2.2. Transition pressure

In H_2–H_2O demixing, the slope of the adiabat of the planet tends to be steeper than the slope of the demixing curve, and the latter changes little with Z. Therefore, both keep diverging for higher Z values along the adiabat. While the temperature along the adiabat can be reduced through enhancement of Z, this is efficient only in the < 0.1 GPa region (see Fig. 2b). Once pressures of the order of a few gigapascals are reached, the temperature along the adiabat is less affected by changes in Z. Therefore, no deeper equilibrium point exists. The rain region will be thin, and therefore characterised by a sharp water-poor-water-rich transition. This is different from the case of H-He demixing, where higher He-abundances lead to warmer demixing curves $T_{\mathrm{dmx}}(P, Y)$ as shown in Nettelmann et al. (2015). In that case, there can be a zone below the onset pressure of demixing where higher equilibrium He-abundances can be found at higher P–T values along the adiabat, and thus the He-poor/He-rich transition becomes gradual (Nettelmann et al. 2015; Mankovich et al. 2016; Howard et al. 2024).

We show the tangential behaviour for the seven phase boundaries in Fig. 7 and under the conditions of a young, warm planet, where demixing is just about to begin.

In the three SFB-linear cases, the intersection between the adiabat and the demixing curve occurs at the cut-off pressure due to the steep (linear) slope and abrupt drop of the demixing curves at higher pressures (Fig. 7a). In these cases, demixing starts at $T_{1\,\mathrm{bar}} \approx 250$ K for 3 GPa, 273 K for 4 GPa, and 310 K for 5 GPa for an initial water abundance of 0.7 that is homogeneous throughout the planet.

With the three phase curves based on the V23 data, the planet adiabat for the equilibrium abundance and the demixing curve is tangential at pressures of $P_Z \sim 4$ GPa. Upon cooling, P_Z remains nearly constant. This is because although Z decreases with $T_{1\,\mathrm{bar}}$ (Fig. 6), the cooling effect on the adiabat with $T_{1\,\mathrm{bar}}$ (Fig. 2a) is compensated by the warming effect due to decreasing Z (Fig. 2b), and the demixing curve changes little with Z. Assuming 0.7 as the initial homogeneous water abundance, H_2–H_2O phase separation starts at $T_{1\,\mathrm{bar}} = 262$ K for the V23 flat case, at 260 K for V23 conv-1800 K, and at 268 K for V23 conv-2000 K (see Fig. 7b).

Only for the Berg24 phase diagram do we observe a different behaviour. Here, the region where the adiabat corresponding to the equilibrium abundance is tangential to the phase boundary extends over a pressure range of 4–11 GPa. Therefore, the rain-out region is wider but homogeneous. Any change in water abundance will occur at pressures deeper than P_Z. Because of this extended region, in the Berg24 case P_Z refers to the end of the tangential region. Higher water abundances in the deep interior will not be on the phase boundary and must therefore be due to other factors such as the formation process. Since there are no further equilibrium points at higher pressure, the water-poor-water-rich transition must be sharp if caused by the H_2–H_2O phase separation. For the Berg24 phase diagram, demixing starts at 261 K (Fig. 7c). For lower initial water abundances, the onset of demixing would occur later, i.e. at lower $T_{1\,\mathrm{bar}}$ values.

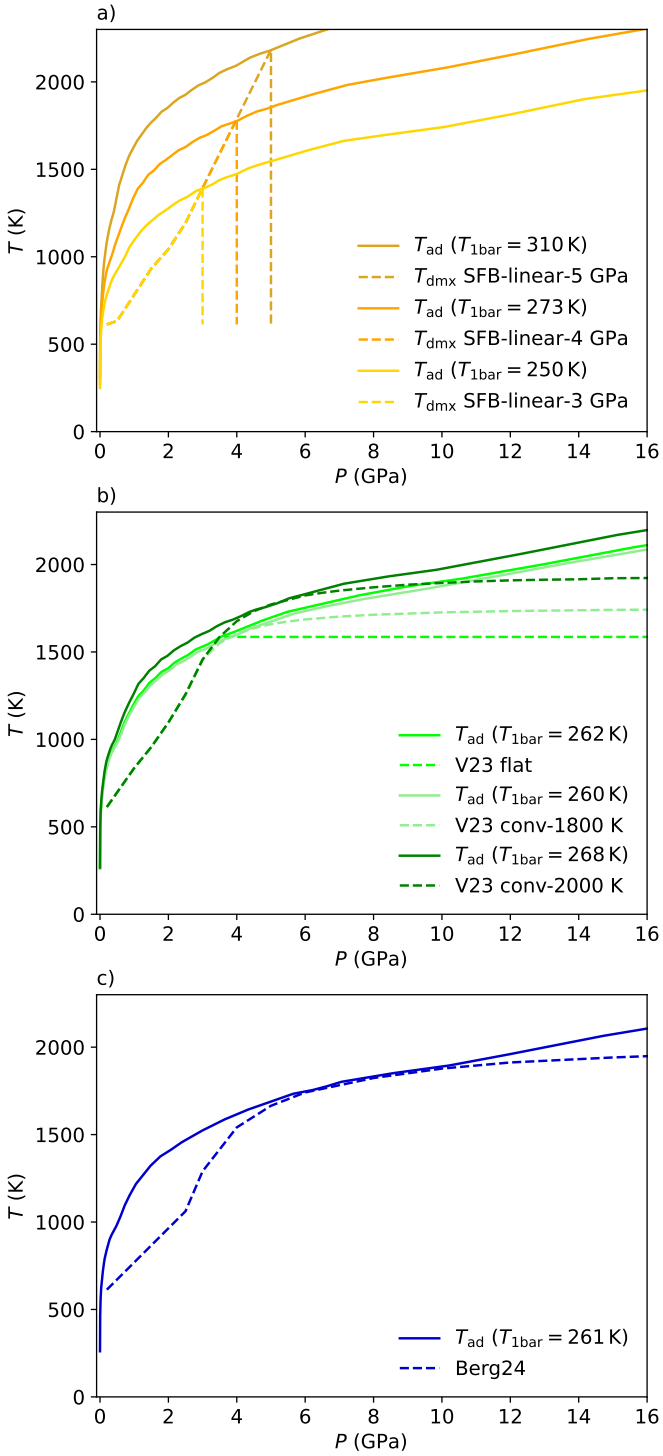

Fig. 7. Adiabats (solid lines) and demixing curves (dashed) for the seven phase diagrams at the onset of demixing. All adiabats and demixing curves are for $Z = 0.7$. (a) SFB-linear-3, 4, 5 GPa; (b) V23-flat (lime), V23 conv-1800 K (light green), V23 conv-2000 K (dark green); (c) Berg24.

3.2.3. Deep-Z level over time

We find that the increase in the deep water abundance in envelope 2 due to the rain-out from the outer layer is negligible. The deep interior water abundance remains essentially primordial. This is a consequence of the low mass of the outer envelope.

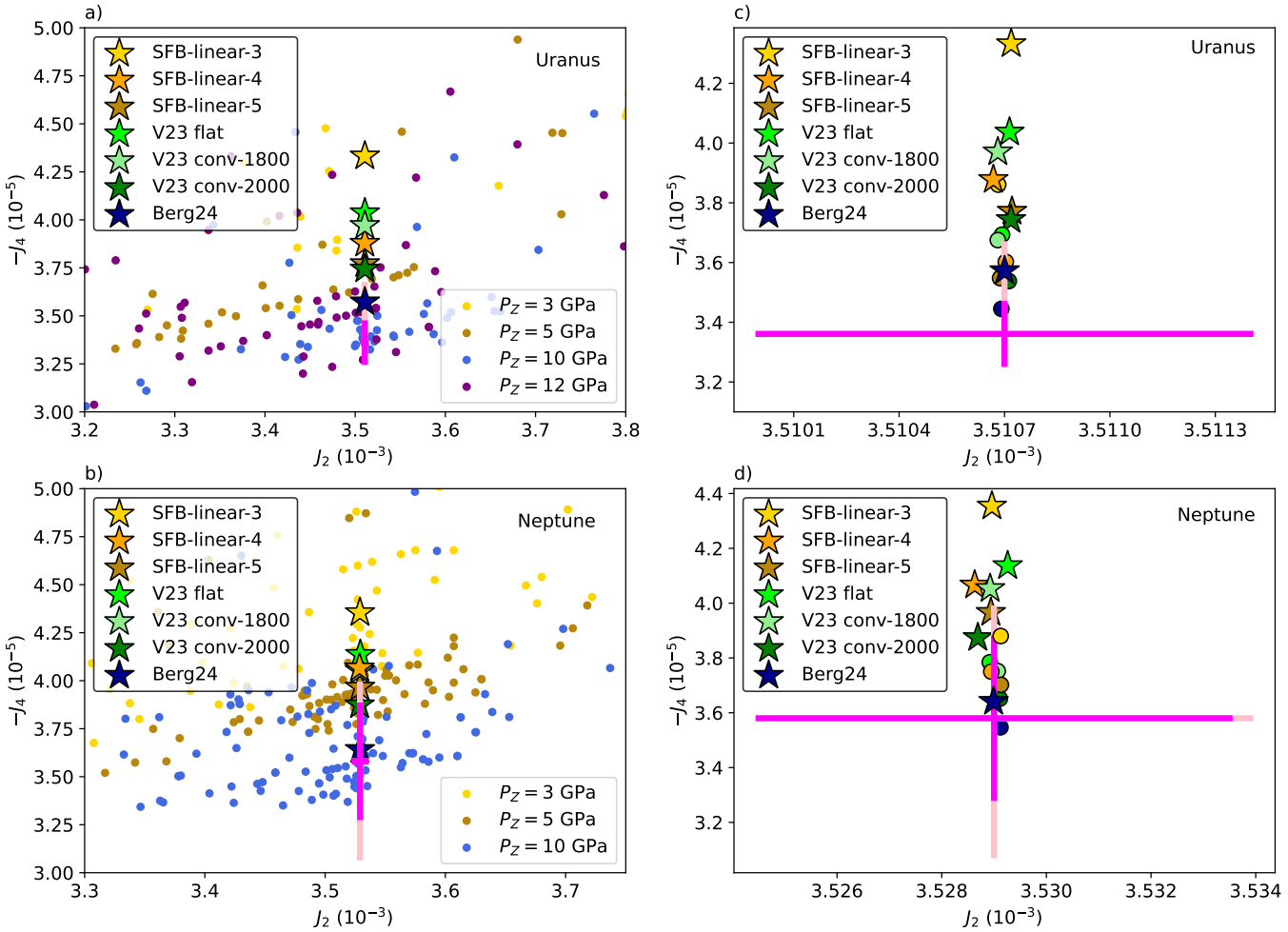

Fig. 8. Gravitational harmonics J_2, J_4 for Uranus (a) and Neptune (b) in case (ii) models (stars) and case (iv) models (dots). The colour of the dots indicates the parameter P_Z. The colour of the stars indicates the H_2–H_2O phase diagram used. Dark pink crosses show observed values. Light pink crosses are wind-corrected static J_4 values (see text for details). In the case of Neptune, the V23 conv-1800 K and SFB-linear-4 GPa stars overlap. We note the change in units for J_2 and J_4 with respect to Table 1. Panels c and d show stars which are the same models as in (a) and (b), and circles: case (iii) models. This figure shows that a mixture of rocks (circles) in the deep interior below the 2000 K level, and water reduces the resulting $|J_4|$ values.

In present-day Neptune, for instance, the 4 GPa level occurs at 0.975 of Neptune's mass.

4. Models constrained by gravitational harmonics

In this section, we describe the already mentioned models where the deep interior abundance is constrained by the gravitational harmonic J_2 in addition to the constraints on $Z_{\rm atm}$ and P_Z from the phase diagrams. Case (ii) models assume water only for heavy elements in the deep envelope, and case (iii) models have both water and rocks in the deep interior above the core at a 0.5x solar ice-to-rock (I:R) ratio, except in the case of Neptune using the Berg24 data, where 0.5 did not provide a solution and we therefore used the I:R of 1x solar. Case (iv) models are constrained by J_2 only. Results for these models are presented in Sect. 4.4. In all of these cases, the rock core mass is a free parameter that is used to adjust $M_p(R_p)$ to the values of Uranus and Neptune.

4.1. Case (ii) and case (iii) models

These models are constrained by $Z_{\rm atm}$ and P_Z from H_2–H_2O phase separation, as explained in the previous section, and by the observed gravitational harmonic J_2. The composition of the deep interior must be determined in order to satisfy the latter constraint. To this end, we introduce two model series, one for an ice-rich composition, case (ii), and another for an ice-rock composition, case (iii).

In case (ii), we confined rocks to the core and assumed that water was the only heavy component present in the deep envelope, i.e. $Z_2 = Z_{\rm H_2O}$. We varied Z_2 to fit J_2 and then checked how well models that satisfied this constraint could also match the observed gravitational harmonic J_4. The seven constrained models of this class are marked by star symbols in Fig. 8.

In case (iii), we also allowed rocks to be present in envelope 2, which substantially reduced the resulting I:R ratio of the models. According to the condensation curves of $MgSiO_3$ and $MgSiO_4$, a condensation temperature of 2000 K occurs at 0.1 GPa and changes only slowly with pressure (Visscher & Moses 2011). Since condensation temperatures generally rise with pressure, extrapolation to higher pressures suggests that 2000 K is a lower limit to the condensation temperatures in giant planets. We thus used 2000 K as an approximate level of silicate clouds and considered rocks only below this temperature. The adiabats of Uranus and Neptune reach 2000 K at pressures of

about 8–15 GPa. In this series of models, we fix the I:R ratio at 0.5× (or 1×) solar for a solar I:R of 2.7.

To compute the gravitational harmonics, we used the MOGROP code (Nettelmann et al. 2012) based on the theory of figures up to the fourth order (Zharkov & Trubitsyn 1978). We checked that using the theory up to the seventh order does not influence the inferred Z_2 values to any significant digits. For consistency with TATOOINE, which employs the AQUA water EoS (Haldemann et al. 2020), we used TATOOINE's adiabats up to P_Z as input to the MOGROP code. Beyond P_Z, we used the H_2O-REOS for water and H/He-REOS.3 for H and He (Becker et al. 2014).

4.2. Case (iv) models

In these models, the abundances of envelopes 1 and 2 above the core (Z_1, Z_2), I:R ratio, and P_Z were all free parameters. These models are only constrained by planetary mass (M_p), radius (R_p), rotation rate, and surface temperature ($T_{1\,\mathrm{bar}}$). In models with rotational flattening, R_p means that the models fit the literature value for the equatorial radius (R_{eq}) at the 1 bar reference level, which is 25 559±4 km for Uranus and 24 764±15 km for Neptune (Lindal et al. 1987; Lindal 1992). Due to their flexibility, these models are well suited for studying how the gravitational harmonics vary in response to variations of single parameters. We present such a parameter study in Fig. A.1.

4.3. Observed gravitational harmonics

For Uranus and Neptune, the lowest order harmonics J_2 and J_4 have been observed by the Voyager 2 spacecraft. Long-term monitoring of the orbital positions of their natural satellites allowed those values to be substantially refined. Here, we used the observed values of $J_2 = (3510.7 \pm 0.7) \times 10^6$ and $J_4 = (-33.61 \pm 1.0) \times 10^6$ for Uranus, and $J_2 = (3529.4 \pm 4.5) \times 10^6$ and $J_4 = (-35.8 \pm 2.9) \times 10^6$ for Neptune (Helled et al. (2010b) and Nettelmann et al. (2013) as based on Jacobson (2009) and Lindal (1992)). These observed values are shown in dark pink in Fig. 8. However, these values are influenced by the zonal winds in the dynamical atmospheres of Uranus and Neptune, whilst here we only compute the static contributions. Kaspi et al. (2013) constrained the depth of winds by decomposing the gravity harmonics into a static and a dynamical contribution. The latter arises from perturbations to the density by the winds, which influence the gravity field. They estimated the dynamical perturbation by comparing their J_4 static values from wind-free interior structure models with the observed J_4. Therefore, in Fig. 8 we also show wind-corrected static values in light pink, whereby we subtracted the dynamic contributions obtained by Kaspi et al. (2013) from the observed values. Table 1 summarises the observed and wind-corrected J_2 and J_4 values we used. While for Jupiter the wind correction is tightly constrained thanks to the measurement of odd harmonics (Kaspi et al. 2020) and leads to a lower static $|J_4|$ value, for Uranus and Neptune the wind-correction is solely inferred from the possible range obtained from interior models, and at present, it acts to enlarge the uncertainty in the static values.

Table 1. Observed, wind-corrected gravitational harmonics J_2 and J_4 and dynamical correction.

Description	$J_2/10^{-6}$	$J_4/10^{-6}$	Reference
Observed-U	3510.7 ± 0.7	–33.61 ± 1	Helled et al. (2010b)
Observed-N	3529.4 ± 4.5	–35.80 ± 2.9	Helled et al. (2010b)
Dyn. corr.-U	–	$-1 \leq \Delta J_4 \leq +3$	Kaspi et al. (2013)
Dyn. corr.-N	–	$-5 \leq \Delta J_4 \leq +4$	Kaspi et al. (2013)
Static-U	3510.7 ± 0.7	–32.61 to –36.61	This work
Static-N	3529.4 ± 4.5	–30.80 to –39.80	This work

Notes. Values are for R_{eq} at 1 bar, as used by Helled et al. (2010b) and Nettelmann et al. (2013) based on Lindal (1992) and Jacobson (2009). Wind corrections from Kaspi et al. (2013) are stated, and the range of corrected static J_4 shown in bright pink in Fig. 8 is given.

4.4. Results

4.4.1. Gravitational harmonics

In Figs. 8a and 8b, we plot the gravitational harmonics J_2, J_4 of our seven case (ii) models (star symbols) and of several hundred case (iv) models for Uranus and Neptune with randomly selected parameters (dots). Figures 8c and 8d show a zoomed-in view to help compare case (ii) models (stars) with case (iii) models (circles).

The choice of P_Z (colour-coded) in the case (iv) models imposes a diagonal lower limit in the $|J_4|$-J_2 plane. This lower limit decreases with increasing P_Z. This means that deeper water-poor to water-rich transitions reduce the $|J_4|$ value at a given J_2, a behaviour that is well-known for Jupiter models (Nettelmann 2011). Above that lower limit, the solutions for different P_Z overlap. An upper limit is expected to occur the more homogeneous the planet is assumed to be (i.e. for higher values of Z_1). However, we have not explored the full parameter space far away from the observed J_4 values.

For Uranus, case (iv) models suggest that if a sharp compositional boundary exists, it should be deeper than 3 GPa, as the models for 3 GPa lie above the J_4 value be they wind-corrected or not. Models with P_Z at 5 GPa (brown) cross the upper limit of the wind-corrected J_4 values. However, to reach the ultimate lower limit of the wind-corrected $|J_4|$, water-poor to water-rich transitions deeper than 10 GPa would be needed. For Neptune, the much larger observational uncertainty in J_4 permits models with $P_Z = 5$ GPa.

This behaviour with P_Z is well reflected in the three case (ii) models with cut-off pressures at 3, 4, and 5 GPa; while the SFB-linear-3 GPa Uranus model (yellow star) is outside the uncertainty range in J_4, the SFB-linear-5 GPa model (brown star) is close to the upper limit of $|J_4|$.

The deepest P_Z is obtained for the Berg24-constrained model. Its J_4 values for Uranus and Neptune are well within the uncertainty range. Thus, the Berg24 model (blue star) permits a classical ice giant interior, where the water-poor to water-rich transition is caused by H_2–H_2O phase separation.

In the case (ii) series, and in agreement with previous three-layer structure models (Nettelmann et al. 2013; Bailey & Stevenson 2021), we find a water-rich deep interior with $Z_2 = Z_{H_2O}$ ranging from [0.68–0.87] for Uranus and [0.73–0.90] for Neptune. These results show that models where the atmospheric water abundances and the transition pressures are constrained by H_2–H_2O phase separation match the known gravity field of Uranus if $P_Z \gtrsim 10$ GPa, and for Neptune if $P_Z \gtrsim 5$ GPa. The constraints and resulting J_4 values of the case (ii) star models are listed in Table 2.

The classic models of the ice giants with interiors highly enriched in water and with a high I:R ratio may not be realistic. In the case (iii) series of models, we investigated the effect

Table 2. Case (ii) and case (iii) constrained models with resulting J_4 values and required water and rock abundances and core mass.

Planet	Phase diagram	Z_{atm}	P_Z (GPa)	Z_{2,H_2O} case (ii)	$J_4/10^{-6}$ case (ii)	M_{core} (M_E)	Z_{2,H_2O} case (iii)	$Z_{2,rocks}$ case (iii)	$J_4/10^{-6}$ case (iii)	M_{core} (M_E)
U	SFB-linear-3 GPa	0.209	3	0.683	–43.32	4.134	0.437	0.324	–38.61	2.252
U	SFB-linear-4 GPa	0.058	4	0.775	–38.78	2.953	0.449	0.332	–36.01	1.777
U	SFB-linear-5 GPa	0.057	5	0.799	–37.71	2.582	0.455	0.337	–35.48	1.556
U	V23 conv-1800 K	0.133	4.8	0.759	–39.70	3.165	0.447	0.331	–36.75	1.870
U	V23 conv-2000 K	0.085	6	0.808	–37.43	2.431	0.458	0.339	–35.38	1.428
U	V23 flat	0.114	3.7	0.743	–40.36	3.397	0.443	0.328	–36.93	1.989
U	Berg24	0.141	11	0.864	–35.72	1.467	0.479	0.355	–34.45	0.654
N	SFB-linear-3 GPa	0.159	3	0.734	–43.54	5.389	0.454	0.336	–38.80	3.332
N	SFB-linear-4 GPa	0.058	4	0.793	–40.66	4.517	0.460	0.341	–37.50	3.057
N	SFB-linear-5 GPa	0.057	5	0.814	–39.66	4.142	0.465	0.344	–37.02	2.838
N	V23 conv-1800 K	0.094	4.8	0.796	–40.53	4.439	0.461	0.341	–37.52	2.996
N	V23 conv-2000 K	0.057	6	0.834	–38.74	3.771	0.471	0.349	–36.51	2.591
N	V23 flat	0.078	3.7	0.778	–41.36	4.756	0.457	0.339	–37.84	3.162
N	Berg24	0.101	11	0.892	–36.41	2.524	0.635(*)	0.235(*)	–35.47	1.880

Notes. In case (ii), the heavy element is only water, whereas in case (iii) rocks are added. Z_{2,H_2O} is obtained as $Z_{2,rocks} \times$ I/R. (*)I/R=1x solar.

of adding rocks to the deep envelope on J_4. We set the I:R factor to 0.5 times the solar value (or 1x) and varied Z_{2,H_2O} and, consequently, $Z_{2,rocks}$. Exploring the full range of I:R factors is out of the scope of this work. Figures 8c and 8d display such models (circles) together with the seven stars of case (ii). The stronger central condensation of mass in case (iii) models tends to reduce $|J_4|$ and to provide a better fit. Moreover, due to the presence of rocks, a lower water abundance in the deep interior is needed. In these case (iii) constrained models, we find solutions with Z_{2,H_2O} in the [0.44–0.48] range and $Z_{2,rocks}$ in the [0.32–0.36] range for Uranus; similarly, we find Z_{2,H_2O} = [0.45–0.64] and $Z_{2,rocks}$ = [0.34–0.24] for Neptune.

4.4.2. Adiabatic gradient

Phase separation and the associated change in the abundances will affect the planetary P–T profile and thus the adiabatic temperature gradient, ∇_{ad}, even if the planet remains adiabatic. Recently, Stixrude et al. (2021) and James & Stixrude (2024) considered the possibility of Uranus and Neptune having a growing frozen core, whose size is determined by the transition between the fluid and superionic phase of water. The authors study the influence of this effect on the thermal evolution and tidal dissipation of the two ice giants. For their interior models, they test a range of adiabatic gradients and specific heat but keep their values constant throughout the interior and the evolution. They show that a frozen core growing over time can explain the observed luminosity of Uranus and Neptune, as well as the time-varying tidal dissipation that can explain the evolution/migration of their satellites. They also find that a slightly different range of adiabatic gradient values (and heat capacities) between both planets (see Fig. 9) can match the luminosities of each planet and associate this difference with a difference in composition between the planets (James & Stixrude 2024).

In Fig. 9, we show adiabatic P–T profiles for various 1 bar temperatures that occur during the evolution of the ice giants, and the associated bulk-volume-weighted adiabatic gradient (∇_{ad}) of Neptune. In the underlying structure models, the water abundances in the outer envelopes change due to phase separation. We find that our bulk volumetric ∇_{ad} value for present-day Neptune is lower than the range considered by James & Stixrude (2024). Our lower values result partially from the AQUA-EOS, which yields colder adiabats than H2O-REOS. Moreover, we find that ∇_{ad} changes by about 0.03 over the course of the evolution. This change with time is much larger than the uncertainty range that James & Stixrude (2024) predict in order to fit the luminosities. We also find that ∇_{ad} changes within the interior, with larger values further out and smaller values deeper inside. Our results suggest that if ∇_{ad} is used to fit luminosity to infer internal composition, the full composition and time-dependent profile should be used because the change over time will influence the cooling behaviour.

5. Discussion

5.1. Z_{atm} from H_2–H_2O phase separation versus from models constrained by gravitational harmonics

In our models constrained by H_2–H_2O phase separation, Z_{atm} is the equilibrium water abundance, which is adopted by the entire outer envelope; i.e. $Z_{atm} = Z_A = Z_1$. In contrast, in classical adiabatic structure models, $Z_{atm} = Z_1$ is determined by the fit to the gravitational harmonics. For our models constrained by phase diagrams only, we find that Z_{atm} is necessarily smaller for Neptune than for Uranus simply because Neptune's observed $T_{1\,bar}$ is ~4 K lower than Uranus' $T_{1\,bar}$, and we extend the temperature profile adiabatically from the 1 bar level down to the phase separation region. In classical three-layer structure models (Nettelmann et al. 2013), Z in the outer envelope (Z_1) spans a rather narrow range of 0–0.2 for Uranus and a wider range of 0–0.6 for Neptune. The higher uncertainty in Neptune's Z_1 is mainly due to the higher uncertainty in J_2 and J_4 than for Uranus (Nettelmann et al. 2013; Helled & Fortney 2020). Thus, Neptune could have a lower Z_1 than Uranus in agreement with structure models. However, for the majority of structure models, Neptune's Z_1 is larger than that of Uranus. Bailey & Stevenson (2021) even found an envelope water mole fraction of ~0.01 for all of their Uranus models and of 0.15–0.20 for all of their Neptune models, thus also systematically higher Z_{atm} values for Neptune than for Uranus.

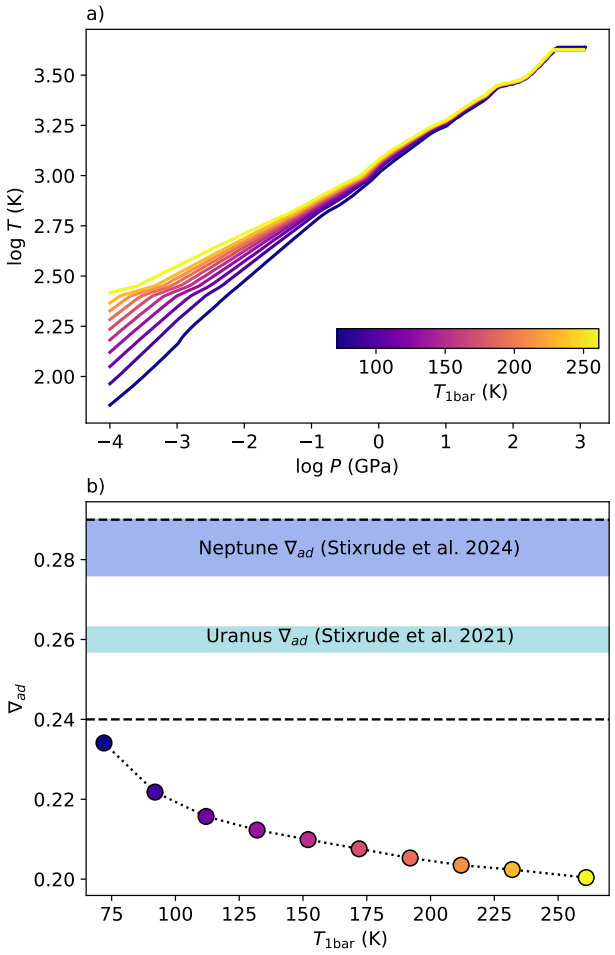

Fig. 9. Comparison of adiabatic gradient obtained from models with phase separation with values used by Stixrude et al. (2021) and James & Stixrude (2024). (a) Interior P–T profiles for Neptune for different $T_{1\,bar}$ temperatures. The metallicity $Z_1 = Z_{atm}$ is varied with $T_{1\,bar}$ according to the Berg24 phase diagram, while Z_2 essentially stays at ∼0.7. (b) Bulk volume-weighted-adiabatic gradient over temperature since the start of demixing (right side of the x-axis) to the present temperature. Blue bands show the range of values for ∇_{ad} found by Stixrude et al. (2021) for Uranus and James & Stixrude (2024) for Neptune to match the cooling times, amongst their range of tested values between 0.24 and 0.29 (dashed lines).

It is unknown whether or not Z_1 in Neptune is higher than in Uranus. If it were indeed higher, and if this Z_1 were due to water, our models would imply that the P–T profiles do not extend adiabatically downwards. Deviation from adiabaticity can arise from inhibition of convection across the methane or the water cloud layer if their abundances are high enough (Guillot 1995; Leconte et al. 2017; Markham & Stevenson 2021), in which case a superadiabatic temperature gradient develops. If that gradient were larger in Neptune than in Uranus, perhaps because of the higher heat flow, Neptune's deep adiabat could be warmer than that of Uranus. As a consequence, phase-diagram-constrained models could then predict a higher Z_1 for Neptune than for Uranus, and in both cases, this Z_1 would differ from the measurable values in their atmospheres due to inhibited convection.

It is also possible that latent heat release from methane or water condensation leads to a colder deep adiabat than seen at the 1-bar level (Kurosaki & Ikoma 2017; Markham & Stevenson 2021). This effect would have to be stronger in Uranus to reduce the temperatures along the deep adiabat more than in Neptune.

Furthermore, with our phase separation model we only addressed the water abundance, while in the actual planets, Z_{atm} is likely composed of methane and other condensable species in addition to water. Our models could then suggest that a higher Z_1 in Neptune's structure models is due to methane rather than water, with Neptune's methane abundance being larger than that of Uranus. However, such a scenario is not supported by current observational data, which find 80 ± 20 solar C/H enrichment in both planets' atmospheres (Atreya et al. 2020).

5.2. Mixing with other elements

Our Z_{atm} values were computed for H-O mixtures according to Eq. (1). In the presence of helium or carbon, which are potentially the most abundant other elements in the atmosphere, the water-mass fraction would decrease, for a given x_{H_2O}/H ratio. Thus, our models predict upper limits on the water-mass fraction. These are $Z_1 = 0.21$ for Uranus and $Z_1 = 0.16$ for Neptune. These upper limits are relevant for the determination of the pressure at the bottom of the water clouds, and the vertical water abundance profile across the cloud up to the top, where the water abundance may be measurable by an entry probe or remote sensing from an orbiter such as Juno for Jupiter.

5.3. Demixing of other elements

Demixing may also occur among other elements in Uranus and Neptune and shape their structures. H–He demixing occurs at megabar pressures (Schöttler & Redmer 2018). In Jupiter, this is the only accepted explanation for its atmospheric He-depletion and even stronger Ne-depletion (von Zahn et al. 1998; Stevenson 1998; Wilson & Militzer 2010). In Saturn, H-He demixing has also been proposed to explain its high luminosity (Fortney & Hubbard 2003; Püstow et al. 2016) and co-axial magnetic field, although there are alternative explanations (Leconte & Chabrier 2013). H–He demixing in Saturn is predicted by all recent theoretical H-He phase diagrams. As the interior of the ice giants is likely even colder than that of the much more massive gas giants, H–He phase separation may also occur in Uranus and Neptune, unless their deep interiors do not contain an H-He gas or the deep interior is shielded by a strong thermal boundary layer (TBL) (Scheibe et al. 2021; Nettelmann et al. 2024), which may result from the water-poor to water-rich transition (Nettelmann et al. 2016; Scheibe et al. 2021) or from the reduced convection in a frozen core (Stixrude et al. 2021; James & Stixrude 2024).

A strong TBL would also influence possible demixing between H and C, which diamond-anvil-cell experiments find to occur at pressures of ∼30 GPa (Watkins et al. 2022), while in laser-shock-compression experiments it is not seen before megabar pressures are reached (Kraus et al. 2017); although, the presence of water appears to support diamond formation at intermediate pressures (He et al. 2022). C-H demixing will act to enrich the atmosphere in H, while C would form diamonds that sink downward. The process of C–H demixing could leave behind a water-rich envelope as assumed in many three-layer models. At present it is still unclear how mixtures of H–He–C–O behave at high pressures.

Further elements that may shape the structure of the ice giants and, perhaps even more so, warm Neptune-like planets, are Mg and Si from the rock-forming refractory elements. Mixing is experimentally seen in the Mg–O–H system under ice giant conditions around 20–30 GPa and 2000 K (Kim et al. 2021), while in numerical simulations mixing is seen around 174 GPa and 6000 K (Kovačević et al. 2023). It is clear that

further studies on the (de)mixing behaviour in H–He–CNO–Mg–Si systems are needed to advance our understanding of Neptune-like planets.

5.4. A possible gradual transition

We find that the water-poor-water-rich transition is sharp because all our constructed phase diagrams assume that the shape of the demixing curve $T_{\rm dmx}(x_{\rm H_2O})$ at 0.2 GPa also holds at higher pressures. In contrast, isobaric H-He demixing curves have a more complex shape (see the phase diagram by Schöttler & Redmer (2018)), so phases of moderate compositional differences (He-enriched, He-depleted) are possible, with compositions that are highly sensitive to temperature (Chang et al. 2024). Should such behaviour also apply to the O–H system at pressures of a few GPa rather than the flat shape we adopted (see Fig. 4 and Sect. 2.3) one would also expect a gradual change in the water abundance in the ice giants. Nevertheless, the region of pressures between 4–10 GPa is narrow, and therefore a potential gradual transition would be much narrower than the He-rain region in gas planets, where it may extend over several hundred GPa (Nettelmann et al. 2015; Chang et al. 2024; Howard et al. 2024). Whether or not a gradual transition is possible that suppresses convection and leads to a warmer interior is at present unknown.

5.5. In the event of no phase separation

Let us suppose H_2–H_2O phase separation does not occur in the ice giants. The low-density outer envelope in Uranus found in structure models would then require a different explanation. Formation models predict a gradual decrease of the heavy-element abundance in the accreted material with time, leading to an outwardly decreasing Z (Helled & Stevenson 2017). However, formation models do not predict a sharp transition from water-poor to water-rich at about 0.85–0.9 of the ice giants' radii unless a very specific formation path is assumed (Venturini & Helled 2017). We may thus assume that the water abundance extends homogeneously down through the atmosphere before it gradually increases, with water being mixed with rocks deeper in the planet. Furthermore, an extended homogeneous, convective, and electrically conductive region such as the ionic water region is required for a dynamo to operate (Stanley & Bloxham 2004, 2006). Therefore, in a fully inhomogeneous planet where a Z gradient inhibits convection, it is unclear how the observed magnetic field could be generated. If the low water abundance found for the outer envelope extended deeper, then another candidate for a sharp increase in Z would be needed. This could be due to rock clouds at about 2000 K and 20 GPa. Alternatively, rocky material may be confined to the deeper layers because accreted rocky planetesimals ablate less efficiently than icy ones. This could lead to a compositional rock-gradient.

5.6. Predictions from formation models

Assessing our atmospheric water abundance estimates in the frame of formation models is somewhat entangled given (a) that the constraints to these models are based on interior structure model estimates, and (b) the various hypotheses of formation currently being investigated. The standard scenario of core accretion (Pollack et al. 1996) seems to support the heavy element amount thought to be in the ice giants, but the in situ formation timescales are much longer than planetary disc lifetimes. Although this timescale issue can be surpassed by using higher accretion rates, matching the constraints from structure models, more specifically the H/He and heavy element estimates, becomes the issue as shown by Helled & Bodenheimer (2014), as well as explaining why Uranus and Neptune did not undergo runaway gas accretion and became gas giants. This all leads to the need for very particular conditions to meet the available requirements, hence a fine-tuning issue.

In the frame of formation models based on pebble accretion, following the pebble accretion rate from Lambrechts et al. (2014), Valletta & Helled (2022) found that Uranus and Neptune may have been formed in situ within the lifetime of protostellar disks. To validate their models, they focus on Uranus and Neptune accreting H/He envelopes as estimated by structure models by Helled et al. (2010a) and Nettelmann et al. (2013). Valletta & Helled (2022) then obtained certain formation scenarios that match the timescales and the H/He mass, and also have a low outer envelope heavy element metallicity (in their case, this is pure water) of a 0.03 mass fraction (see Fig. 6). Their estimate is not far from our water-depleted atmosphere estimates. Valletta & Helled (2022) find, however, that apart from these successful cases, in many others the planets must have accreted an extra amount of heavy elements after their formation (e.g. through giant impacts) to account for the missing heavy elements inside.

Moreover, Mousis et al. (2024) use the high carbon enrichment observed in the atmospheres of Uranus and Neptune (Atreya et al. 2020) and the suggestion of Ali-Dib et al. (2014) on the possible formation of the ice giants at the CO line to estimate the evolution and abundances of certain species in this region. We converted their estimates of bulk envelope oxygen enrichments with respect to protosolar ones. These are also shown in Fig. 6. Given that these are bulk estimates, and therefore different to our $Z_{\rm atm}$, we do not compare our results to these estimates directly.

6. Summary and conclusions

Based on the presented results, we draw the following conclusions:

- We constructed seven phase diagrams based on experimental data up to 4 GPa and theoretical data up to 12 GPa that span the current level of uncertainty. In all cases, we obtain an overlap with the adiabats of Uranus and Neptune. This leads to a strong rain-out of water in the planets;
- Assuming no barrier between the atmosphere and the region of phase separation, we predict a low atmospheric water mass fraction abundance $Z_{\rm atm}$ of 0.05–0.21 for Uranus and of 0.05–0.16 for Neptune;
- The resulting water-poor to water-rich transition is sharp, and it occurs between P_Z = 4 and 11 GPa, depending on phase diagram uncertainties;
- Structure models constrained by the $Z_{\rm atm}$ and P_Z from H_2–H_2O phase separation fit J_2. Whether or not the models also fit J_4 strongly depends on P_Z. For phase diagrams with $P_Z \lesssim 4$ GPa, the resulting $|J_4|$ values are too large for both Uranus and Neptune, while for phase diagrams with $P_Z \gtrsim 10$ GPa (Uranus) or 5 GPa (Neptune), the upper limit of the wind-corrected $|J_4|$ values is reached. The demixing curve of Bergermann et al. (2024) leads to the deepest P_Z and works for both planets;
- Structure models with rocks below an assumed rock cloud condensation level at 2000 K (or deeper) have lower $|J_4|$ values; so, the observed mean values can be reached, suggesting that true low $|J_4|$ values could indicate a deeper

rock-poor/rock-rich transition. Reduced uncertainties in the observed J_4 and the wind contribution of both Uranus and Neptune are needed to rule out or support the presented models;
- The adiabatic gradient changes by ∼10% over time. This change is expected to influence the cooling of the planet;
- The H-O system may not be the only relevant one that shapes the interior structure of the ice giants. In the C-H system, demixing has also been found in both experiments and in simulations. Different systems may have different separation locations, effectively leading to gradual Z-transitions, where convection can be suppressed;
- The sinking of water releases gravitational energy and leads to the expansion of the then less dense outer envelope. While the effect is likely small, it should be quantified and compared to the low luminosity of Uranus in future work;
- Future work using evolution models will provide a more complete picture of the consequences of this process on the internal structure and thermal evolution of the planets.

The ice giant community is making efforts to design a space mission to explore the ice giants (e.g. Fletcher et al. 2020). The Decadal Survey National Academies of Sciences Engineering and Medicine (2023) emphasised the many open questions regarding our understanding of their formation, interior structure, and evolution and proposes a Uranus Orbiter and Probe (UOP) as NASA's next flagship mission with the highest priority. We of course hope that this will indeed become a reality and want to emphasise the direct relation between the work presented here and the decadal study question 7 (specifically 7.1 and 7.2). Obtaining new gravity-field data would be crucial in this case, and extremely helpful for setting a constraint on the possible deep water abundance. Furthermore, in situ abundance measurements from an atmospheric probe would result in more constraints on the volatile abundances, bringing us a step closer to understanding what the interior composition of these planets looks like.

Acknowledgements. We acknowledge the support of the German Science Foundation (DFG) through the research unit FOR 2440 "Matter under planetary interior conditions" (projects PA 3689/1-1 and NE 1734/2-2). N.N. acknowledges support through NASA's Juno Participating Scientist Program under grant 80NSSC19K1286. We also thank the reviewer for their thorough feedback.

References

Ali-Dib, M., Mousis, O., Petit, J.-M., & Lunine, J. I. 2014, ApJ, 793, 9
Atreya, S., Hofstadter, M., In, J., et al. 2020, SSRv, 216, 18
Bailey, E., & Stevenson, D. J. 2021, Planet. Sci. J., 2, 64
Bali, E., Audétat, A., & Keppler, H. 2013, Nature, 495, 220
Baumeister, P., & Tosi, N. 2023, A&A, 676, A106
Baumeister, P., Padovan, S., Tosi, N., et al. 2020, ApJ, 889, 42
Becker, A., Lorenzen, W., Fortney, J. J., et al. 2014, ApJS, 215, 21
Bergermann, A., French, M., & Redmer, R. 2021, PCCP, 23, 12637
Bergermann, A., French, M., & Redmer, R. 2024, Phys. Rev. B, 109, 174107
Bolton, S., Lunine, J., Stevenson, D., et al. 2017, Space Sci. Rev, 213, 5
Chabrier, G., & Debras, F. 2021, ApJ, 917, 4
Chabrier, G., Mazevet, S., & Soubiran, F. 2019, ApJ, 872, 51
Chang, X., Chen, B., Zeng, Q., et al. 2024, Nat. Commun., 15, 8543
Fletcher, L. N., Helled, R., Roussos, E., et al. 2020, Planet. Space Sci., 191, 105030
Fortney, J. J., & Hubbard, W. B. 2003, Icarus, 164, 228
Guillot, T. 1995, Science, 269, 1697
Haldemann, J., Alibert, Y., Mordasini, C., & Benz, W. 2020, A&A, 643, A105
He, Z., Rödel, M., Lütgert, J., et al. 2022, Sci. Adv., 8, eabo0617
Helled, R., & Bodenheimer, P. 2014, ApJ, 789, 69
Helled, R., & Stevenson, D. 2017, ApJ, 840, L4
Helled, R., & Fortney, J. J. 2020, Philos. Trans. Roy. Soc. Lond. A, 378, 20190474
Helled, R., Anderson, J. D., Podolak, M., & Schubert, G. 2010a, ApJ, 726, 15
Helled, R., Anderson, J. D., & Schubert, G. 2010b, Icarus, 210, 446
Helled, R., Nettelmann, N., & Guillot, T. 2020, Space Sci. Rev., 216, 38
Howard, S., Müller, S., & Helled, R. 2024, A&A, 689, A15
Hubbard, W. B., & MacFarlane, J. J. 1980, J. Geophys. Res., 88, 225
Hubbard, W., & Marley, M. S. 1989, Icarus, 78, 102
Iess, L., Militzer, Kaspi, Y., Nicholson, P., et al. 2019, Science, 364, 2965
Jacobson, R. A. 2009, AJ, 137, 4322
James, D., & Stixrude, L. 2024, Space Sci. Rev., 220, 21
Kaspi, Y., Showman, A. P., Hubbard, W. B., Aharonson, O., & Helled, R. 2013, Nature, 497, 344
Kaspi, Y., Galanti, E., Showman, A. P., et al. 2020, Space Sci. Rev., 216, 84
Kim, T., Chariton, S., Prakapenka, V., et al. 2021, Nat. Astron., 5, 815
Kovačević, T., González-Cataldo, F., & Militzer, B. 2023, Contrib. Plasma Phys., 63, e202300017
Kraus, D., Vorberger, J., Pak, A., et al. 2017, Nat. Astron., 1, 606
Kurosaki, K., & Ikoma, M. 2017, AJ, 153, 260
Lambrechts, M., Johansen, A., & Morbidelli, A. 2014, A&A, 572, A35
Leconte, J., & Chabrier, G. 2013, Nat. Geosci., 6, 347
Leconte, J., Selsis, F., Hersant, F., & Guillot, T. 2017, A&A, 598, A98
Lindal, G. F. 1992, AJ, 103, 967
Lindal, G. F., Lyons, J. R., Sweetnam, D., et al. 1987, J. Geophys. Res., 92, 14987
MacKenzie, Jasmine, Grenfell, John Lee, Baumeister, Philipp, et al. 2023, A&A, 671, A65
Malamud, U., Podolak, M., Podolak, J. I., & Bodenheimer, P. H. 2024, Icarus, 421, 116217
Mankovich, C., Fortney, J. J., & Moore, K. L. 2016, ApJ, 832, 113
Markham, S., & Stevenson, D. 2021, Planet. Sci. J., 2, 146
Militzer, B., Soubiran, F., Wahl, S. M., & Hubbard, W. 2016, J. Geophys. Res. Planets, 121, 1552
Mousis, O., Schneeberger, A., Cavalié, T., et al. 2024, Planet. Sci. J., 5, 173
Movshovitz, N., Fortney, J. J., Mankovich, C., Thorngren, D., & Helled, R. 2020, ApJ, 891, 109
National Academies of Sciences Engineering and Medicine 2023, Origins, Worlds, and Life: A Decadal Strategy for Planetary Science and Astrobiology 2023–2032 (Washington, DC: The National Academies Press)
Nettelmann, N. 2011, Ap&SS, 336, 47
Nettelmann, N., Becker, A., Holst, B., & Redmer, R. 2012, ApJ, 750, 52
Nettelmann, N., Helled, R., Fortney, J., & Redmer, R. 2013, Planet. Space Sci., 77, 143
Nettelmann, N., Fortney, J. J., Moore, K., & Mankovich, C. 2015, MNRAS, 447, 3422–3441
Nettelmann, N., Wang, K., Fortney, J., et al. 2016, Icarus, 275, 107
Nettelmann, N., Cano Amoros, M., Tosi, N., Fortney, J. J., & Helled, R. 2024, Space Sci. Rev., 220, 56
Neuenschwander, B. A., & Helled, R. 2022, MNRAS, 512, 3124
Neuenschwander, B. A., Müller, S., & Helled, R. 2024, A&A, 684, A191
Pearl, J. C., & Conrath, B. J. 1991, J. Geophys. Res. Space Phys., 96, 18921
Pearl, J., Conrath, B., Hanel, R., Pirraglia, J., & Coustenis, A. 1990, Icarus, 84, 12
Podolak, J., Malamud, U., & Podolak, M. 2022, Icarus, 382, 115017
Pollack, J. B., Hubickyj, O., Bodenheimer, P., et al. 1996, Icarus, 124, 62
Püstow, R., Nettelmann, N., Lorenzen, W., & Redmer, R. 2016, Icarus, 267, 323
Scheibe, L., Nettelmann, N., & Redmer, R. 2019, A&A, 632, A70
Scheibe, L., Nettelmann, N., & Redmer, R. 2021, A&A, 650, A200
Schöttler, M., & Redmer, R. 2018, Phys. Rev. Lett., 120, 115703
Seward, T., & Franck, E. 1981, Ber. Bunsenges. Phys. Chem., 85, 2
Stanley, S., & Bloxham, J. 2004, Nature, 428, 151
Stanley, S., & Bloxham, J. 2006, Icarus, 184, 556
Stevenson, D. J. 1998, J. Phys. Condensed Matter, 10, 11227
Stixrude, L., Baroni, S., & Grasselli, F. 2021, Planet. Sci. J., 2, 222
Valletta, C., & Helled, R. 2022, ApJ, 931, 21
Vazan, A., Sari, R., & Kessel, R. 2022, ApJ, 926, 150
Venturini, J., & Helled, R. 2017, ApJ, 848, 95
Visscher, C., & Moses, J. I. 2011, ApJ, 738, 72
Vlasov, K., Audétat, A., & Keppler, H. 2023, Contrib. Mineral. Petrol., 178, 36
von Zahn, U., Hunten, D. M., & Lehmacher, G. 1998, J. Geophys. Res. Planets, 103, 22815
Watkins, E. B., Huber, R. C., Childs, C. M., et al. 2022, Sci. Rep., 12, 631
Wilson, H. F., & Militzer, B. 2010, Phys. Rev. Lett., 104, 121101
Zharkov, V. N., & Trubitsyn, V. P. 1978, Physics of planetary interiors (Pachart Publishing House)

Appendix A: Response of J_2 and J_4 to parameter variation

We present an additional parameter study to inspect the effects of P_Z, as well as the water and rock abundances, on the computed gravity harmonics of Uranus. Figure A.1 shows the dependence of each input parameter whilst the rest remain constant. Decreasing the transition pressure from the water-poor to the water-rich envelope tends to overestimate the harmonics, as shown in Fig. A.1a. This behaviour was seen already in Fig. 8. When only the envelope water abundance is varied, like in Fig. A.1b or c, this also increases J_2 and J_4. Similarly, increasing the amount of rocks in the deeper interior has the same effect.

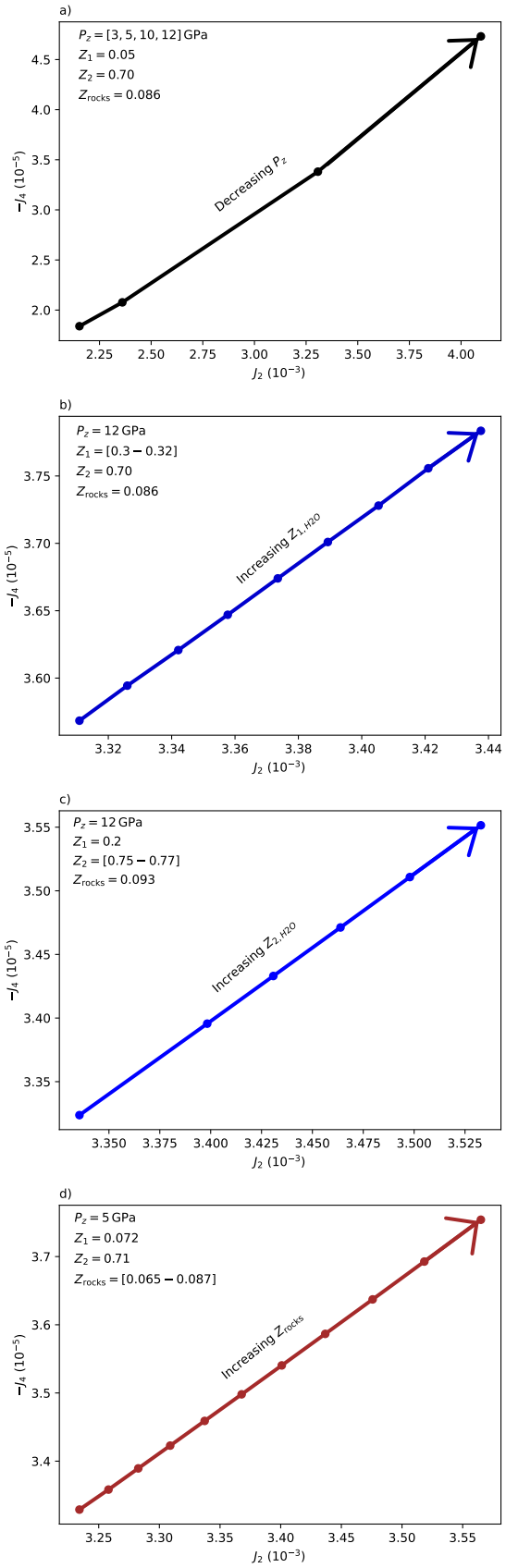

Fig. A.1. Response of the J_2, J_4 to variations of a single parameter of case (iv) models. In plot (a) we keep all abundances constant and only vary P_Z. In (b) we show the behaviour of the harmonics when varying only the top layer water abundance. In (c) we vary deep water abundance as done in case (ii) models and in (d) we vary rock abundance in the deep interior.